INSTITUTO SUPERIOR TÉCNICO
Universidade Técnica de Lisboa

A Bayesian Perfusion estimation using spatio-temporal priors in ASL-MRI

Miguel Lourenço Rodrigues

Dissertation submitted to obtain the Master's Degree in

Biomedical Engineering

Jury

President:	Prof. Fernando Henrique Lopes da Silva
Supervisor:	Prof. João Miguel Raposo Sanches
Supervisor:	Prof. Patrícia Margarida Piedade Figueiredo
External:	Prof. Rita Gouveia Nunes
External:	Prof. Tiago Vaz Maia

December 2011

Acknowledgements

First of all, I would like to thank my advisors, Prof. João Sanches and Prof. Patrícia Figueiredo, for their guidance, tips, hints, notes, corrections and support throughout the long process of making this thesis. They have never stopped supporting me, and for that, I cannot thank them enough.

I also want to leave a word of appreciation to my mother, my father, my brother and sister. Every single one of them has somehow made a critical contribution to realization of this thesis. I can never deny the importance of a warm Sunday breakfast, the perspective given by a piece of advise in the right moment or just a simple goofing time spent together.

To my grandmothers, always so eager to praise the engineer grandson, and to both my grandfathers, João and Vitorino, although no longer among us, definitely always with me.

To Susana, although our story is a roller coaster, I'm sure there are still many years ahead and a lot of space in my bag. Thank you for always being there.

To all my friends, from Ponte de Sôr to as far as Italy and Poland. I have always had the luck to have many good friends, with whom I could always count on.

Although they probably do not understand, I would not feel good with myself if I would not thank the many "4 patas" friends I have. All of them are, without a doubt, sources of happiness.

And finally, my most sincere "thank you" goes to my best friend, Ushy.

Abstract

Arterial Spin Labeling (ASL) is a non-invasive technique for generating perfusion images of the brain. Since it does not require the use of an artificial tracer, it has been significantly gaining recognition as a method for obtaining perfusion parameters. Following an alternating labeling/control acquisition sequence, the minor magnetization difference between labeled and non-labeled images is detected by performing image subtraction. Due to the intrinsically low *Signal to Noise Ratio* (SNR), label/control acquisitions must be repeated a number of times and signal averaging is then performed in order to detect the small perfusion dependent difference signal. In this work, a novel ASL data analysis approach is proposed, in which the averaging procedure is not done explicitly. The magnetization difference estimation problem is formulated in a Bayesian framework, where spatio-temporal priors are used to deal with the ill-posed nature of the estimation task, hence enabling shorter acquisition times, without compromising the estimation quality. The *a priori* assumption that no drastic signal variations are expected along the same tissue, except at the organs boundaries, is imposed by the priors. To evaluate the performance of the proposed algorithm, the results obtained using synthetic data were compared against the two most common subtraction methods used to process ASL data, pair-wise and surround subtraction. The results were very encouraging, as greater SNR was achieved and the overall mean-squared error was highly reduced. The proposed algorithm was then applied to a real data-set, also obtaining satisfactory results.

Keywords: arterial spin labeling, bayesian approach, perfusion, magnetization, spatio-temporal priors.

Resumo

Arterial Spin Labeling (ASL) é um método não invasivo através do qual se obtêm imagens de perfusão do cérebro. Utilizando uma sequência de marcação alternada, a diferença de magnetização entre o conjunto das imagens é obtido realizando subtracção entre as imagens marcadas e não marcadas. Devido ao baixo valor de SNR, é necessário adquirir um número suficiente de imagens que permita detectar a pequena diferença de magnetização à qual se associa a perfusão. Neste trabalho, sugere-se uma nova abordagem ao processamento de imagens de ASL, onde o cálculo da média não é efectuado de modo explícito. Através de uma formulação Bayesiana, onde são aplicados priors espacio-temporais para auxiliar no processo de estimação da imagem, torna-se possível diminuir os tempos de aquisição sem comprometer a qualidade da imagem estimada. A condição *a priori* de que não são esperadas transições de sinal abruptas ao longo do mesmo tecido, excepto nos limites dos orgãos, é imposta pela aplicação dos priors. Para avaliar a performance do algoritmo proposto, os resultados obtidos em simulações com dados sintéticos foram comparados com os dois métodos de subtracção mais usados para processamento de sinal de ASL, *pair-wise subtraction* e *surround subtraction*. Os resultados obtidos foram encorajadores, na medida em que se obteve um aumento de SNR da imagem e uma diminuição do erro médio. Posteriormente aplicou-se o método a dados reais e os resultados obtidos foram igualmente satisfatórios.

Palavras chave: arterial spin labeling, formulação bayesiana, perfusão, magnetização, priors espácio-temporais.

Contents

List of Figures

List of Tables

List of Abbreviations

AWGN	Additive White Gaussian Noise
ASL	Arterial Spin Labeling
BOLD	Blood-Oxygen-Level Dependence
CBF	Cerebral Blood Flow
CT	Computed Tomography
DAI	Double Adiabatic Inversion
EPI	Echo Planar Imaging
EPISTAR	Echo Planar Imaging and Signal Targeting with Alternating Radiofrequency
FAIR	Flow-sensitive Alternating Inversion Recovery
GM	Gray Matter
TI	Time Interval
ME	Mean Error
MRI	Magnetic Resonance Imaging
MT	Magnetization Transfer
MAP	Maximum *a posteriori*
ML	Maximum Likelihood
NMR	Nuclear Magnetic Resonance
pCASL	pseudo-Continuous Arterial Spin Labeling
PET	Positron Emission Tomography
PICORE	Proximal Inversion with a Control for Off-Resonance Effects
PLD	Post Labeling Delay
ROI	Region of Interest
SAR	Specific Absorbtion Rate
SNR	Signal-to-noise Ratio
WM	White Matter

Chapter 1

Introduction

In the introductory Chapter of this work a brief overview on Arterial Spin Labeling is first presented, in Section 1.1, followed by the main motivations that led to the realization of this thesis in Section 1.2. In Section 1.3 the goals of this thesis are set, and in Section 1.4 the original contributions that resulted from it are presented. Finally, Section 1.5 contains an overview on the thesis structure.

1.1 Arterial Spin Labeling

Cerebral Blood Flow (CBF) is a measure of the volume of blood passing through a point in the brain circulation per unit of time and, in a healthy individual, alterations in neural activity lead to changes in local CBF[1]. If the volume of the tissue is taken into account, the *perfusion* can also be measured, as the CBF per unit volume of tissue. In fact, perfusion is the process by which the nutrients in the blood stream are delivered to the tissues through the capillary bed. It is a parameter that provides very useful information about the condition of a certain organ. There are many techniques to assess the previous mentioned hemodynamic parameters, and this work is focused on a technique whose potential is widely recognized: Arterial Spin Labeling (ASL).

In ASL, the blood passing through a determined region (upstream from the region of interest) is labeled with an inversion pulse, and after a certain time interval (TI), the blood reaches the region of interest and an image is acquired. If a control image, where no labeling was performed, is subtracted from the labeled acquisition, the resulting image has a small magnetization difference caused by the exchange of labeled water molecules from the blood to the surrounding tissue, which is an indicator of CBF. Since the magnetization difference is very small, a set of label-control acquisitions has to be performed to obtain an image with sufficient *Signal to Noise Ratio* (SNR). A schematics of ASL imaging is presented in Figure 1.1.

There are several methods for performing this labeling of the arterial blood and also for performing the image subtraction. These will all be addressed in depth in Chapter 2.

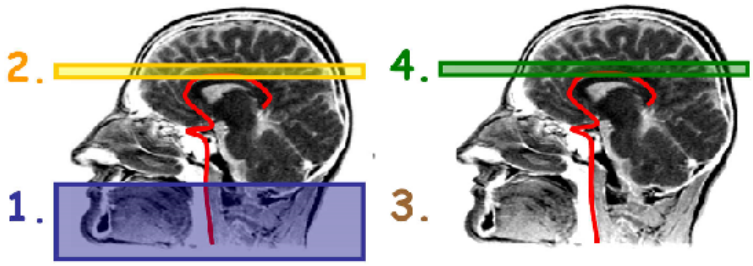

Figure 1.1: ASL acquisition schematic diagram: 1- Labeling of the inflowing arterial blood; 2- After the TI, image is acquired; 3- Control experiment, where no labeling is performed; 4- Image is acquired. The following step is the subtraction of the image acquired in 4 by image acquired in 2. Figure taken from[2].

1.2 Motivations

Nowadays, medicine has become supported by the various imaging methods available and these have become an indispensable part of the diagnostic. However, medical images are often deteriorated by noise from various sources of interference and many other phenomena that affect the measurement processes in imaging and data acquisition systems. In addition, there are cases where the nature of the physiological system under investigation and the procedures themselves further diminish the visibility of the details. Often, the difference between healthy and unhealthy tissues is very small, and can be confused with the noise corrupting the image. For this reason, any improvement in the visual quality may assist the medical specialist interpretation of the image[3].

In the search for the best possible image, one must take into consideration that the processing techniques themselves may increase noise while improving contrast or eliminate small details and edge definition while attempting to remove noise[4].

For the specific case of ASL, a major challenge is to find a way to improve image SNR. One way is to acquire a sufficient number of repetitions of the label/control pairs and subsequently perform signal averaging. However, due to TI required to allow the labeled blood to perfuse into the tissue of interest, relatively long repetition times (TR) are required (typically, around 2 seconds), which may lead to unreasonably long acquisitions[5].

The SNR limitations of ASL imaging, together with its recognized potential serves as the main motivation for this thesis. By using a signal processing model that better copes with the very low image SNR, it is possible to obtain images with better quality while potentially reducing acquisition time.

1.3 Goals

The main goal of this thesis is to propose a new signal processing method, in order to improve ASL image SNR and reduce the overall *Mean Error*(ME), allowing the reduction of the acquisition

times without compromising image quality. It is proposed a new approach, where the averaging procedure is not explicitly done. The signal processing is formulated in a Bayesian framework where spatio-temporal priors are used to deal with the image reconstruction task. It is expected that by the addition of *a priori* knowledge about the image to be reconstructed will improve both parameters previously mentioned.

1.4 Original Contributions

The original contribution of this thesis is the use of a Bayesian approach to estimate the perfusion signal from ASL data, using a priori knowledge of the signal properties, as opposed to the current subtraction approaches.

The work developed in the making of this thesis gave rise to an article entitled "Bayesian perfusion estimation with PASL-MRI", presented as a poster in "RecPad2010 - 16th edition of the Portuguese Conference on Pattern Recognition, UTAD University, Vila Real, October 29th".

1.5 Thesis Structure

The present work is divided in five chapters. In the first Chapter, where this section is included, a small introduction to ASL is presented , as well as the main motivations and goals that led to the realization of this thesis. The Chapter is completed with a section dedicated to the original contributions of this thesis.

Chapter 2 comprises an in depth literature review on ASL and current signal processing methods associated with it.

Chapter 3 consists of an extensive presentation of the problem formulation and the consequent mathematical model considered throughout this work.

The results obtained with the implemented model, as well as a discussion of these results are presented in Chapter 4. This chapter includes a section dedicated to the synthetic data used, as well as one for the real data testing.

Finally, Chapter 5 provides the conclusions of this thesis and the presentation of a few concluding remarks, complemented with ideas considered of interest for future work.

Chapter 2

Literature Review

In Chapter 2 is presented a bibliographic review on ASL.

This Chapter begins with an overview on ASL, addressing the four major types of ASL, in Section 2.1. Section 2.2 presents the current ASL signal processing methods, and closing the Chapter, Section 2.3 introduces some alternative techniques to ASL, and a comparison among them.

2.1 Arterial Spin labeling

Nuclear Magnetic Resonance (NMR), the foundations of ASL, was first discovered in 1946 by Felix Bloch[6] and Edward Purcell[7]. However, it was not until the last two decades that Arterial Spin Labeling - Magnetic Resonance Imaging (ASL-MRI) perfusion technology brought great innovation into human brain function and perfusion imaging.

As previously mentioned, ASL is a non-invasive technique that allows the quantification of brain perfusion, which is a measure of the rate at which nutrients and oxygen are delivered by the blood flow to the tissues in the capillary bed and it is considered to be one of the most fundamental physiological parameters[8, 9]. For instance, perfusion disorders account for most of the leading causes of medical disability and mortality. Furthermore, ASL can provide perfusion maps that can be of great use when interpreting several conditions, such as tumors, acute stroke, chronic cerebrovascular disease, epilepsy and several degenerative diseases[10].

Water protons have a very strong presence in the human body. For instance, the total amount of water in a man of an average weight of 70 kilograms is approximately 40 litres, amounting to 57% of his total body weight[11]. The ASL method consists on the labeling of the water protons present in the blood of the vessels that supply the region to be imaged. After a certain period of time, named *post labeling delay* (PLD), the labeled blood reaches the region to be imaged and then an image is acquired. In order to acquire a control image, the procedure is repeated without the labeling of the blood. It is the subtraction of the control and labeled image that allows the remotion

of static tissue signal, hence allowing the creation of the perfusion image, since the remaining signal is expected to be a relative measure of the perfusion[12].

The signal difference is a very small fraction of the tissue signal (approximately 1-2%) and depends on many parameters, such as flow rate, T1 of the blood and tissue, and transit time for blood to travel from the labeling region to the imaging plane. To make sure that the SNR is sufficiently high to allow for a secure diagnostic review, several sequences of control-labeled images are acquired. A perfusion map can then be obtained by considering the *General Kinetic Model*[13].

The acquisition of an ASL image with an MRI pulse sequence has two independent components, *i.e.* preparation and acquisition components. The preparation component consists in the blood labeling with different magnetic states, in order to create the labeled and control images. The acquisition component refers to the data acquisition. ASL acquisition usually is performed using a fast acquisition method, such as Spiral or Echo Planar Imaging (EPI). The independence between the preparation and acquisition components has allowed researchers to choose the combination that best fits the experiment[12]. In the following Sections, the four different types of preparation components are presented.

2.1.1 Continuous Arterial Spin Labeling

Continuous Arterial Spin Labeling (CASL) was the first ASL model to be proposed[14]. In this first approach, a continuous flow-driven adiabatic inversion scheme is used. The inversion of the arterial blood magnetization is performed using a continuous radio-frequency (RF) pulse (2-4 seconds) while applying a magnetic field gradient in the direction of the flow. A slow variation of the resonance frequency occurs in the moving arterial spins, resulting in their inversion, while the static tissues spin will only be saturated. The efficiency of the inversion is related to several factors, such as the mean velocity of the blood, angles of the vessels to the plane selected, RF amplitude, and gradient strength. The effectiveness of CASL is also affected by an effect occurring in long lasting inversion pulses, called the *Magnetization Transfer* (MT), which may lead to overestimated perfusion[15].

In Figure 2.1 it is presented a representation of a CASL sequence.

2.1.2 Pulsed Arterial Spin Labeling

The Pulsed modality of ASL was first proposed in 1994[16]. PASL uses a short RF pulse (typically between 5 to 20 ms) to invert a thick portion of spins in the proximal plane (10-15 centimeters distance) to the imaging region. Although the duration of the pulse is considerably smaller, the MT effects have to be considered as well. The ease of implementation and reduced practical problems, when compared to CASL, have made PASL a popular choice for perfusion imaging. In fact, this is reflected in the wide range of sequences available today. A representation of a PASL sequence is shown in Figure 2.2.

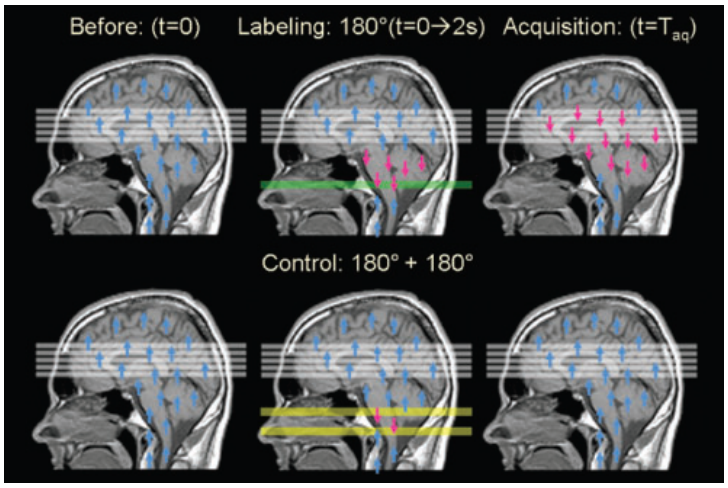

Figure 2.1: A CASL sequence. The top three images represent a labeled acquisition and the bottom three a control. For both sequences, at time $t = 0$ the blood is normally inflowing to the brain, and from $t = 0$ to $t = 2$, in the labeling sequence an inversion pulse (represented by the green square) inverts the magnetization of the spins of the arterial water by 180°. In the same period, for the control experiment, two inversion pulses (represented by the two yellow squares) invert the magnetization of the arterial blood by 180° and then return it to its normal state. Finally, at $t = T_{aq}$, the images are acquired. Adapted from[15].

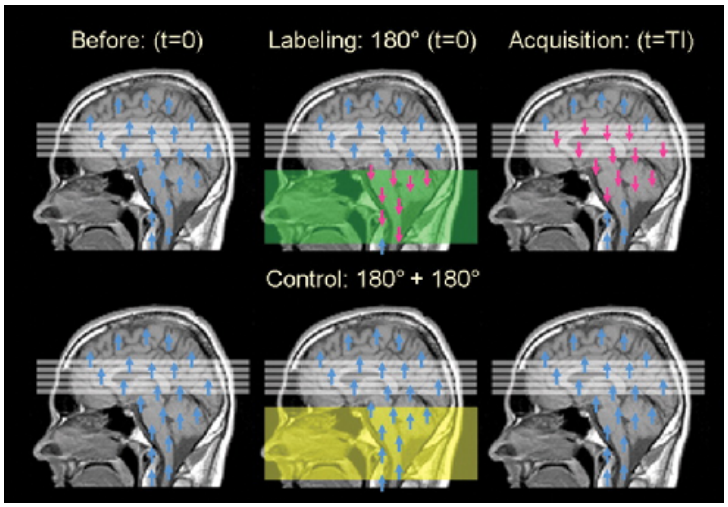

Figure 2.2: A PASL sequence. The top three images represent a labeled acquisition and the bottom three a control. At time $t = 0$ the blood is normally inflowing to the brain, and shortly after $t = 0$ in the labeling sequence, a very small inversion RF pulse is applied to a thick portion of blood (represented by the green square) and inverts the magnetization of the spins of the arterial water by 180°. In the control experiment, the same RF pulse is applied (represented by the two yellow squares) but without the magnetization gradient, hence not inverting the spins. Then, at $t = TI$, the images are acquired[15].

2.1.3 Pseudo-Continuous Arterial Spin Labeling - pCASL

As previously mentioned, CASL has a small efficiency of labeling when compared to PASL. In order to face this disadvantage without raising the RF power deposition, a train of RF pulses in conjunction with a synchronous gradient field can be used to perform a flow-induced adiabatic inversion as in CASL.

Nowadays, pCASL can be performed in two different approaches. The first one is named *unbalanced pCASL*, where the gradients applied between two consecutive RF pulses are non-zero in labeling experiment and zero in control (Figure 2.3).

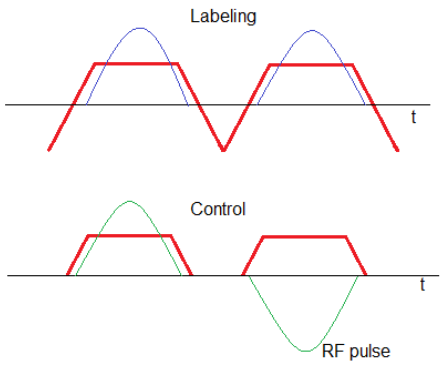

Figure 2.3: A typical unbalanced pCASL experiment.

The second approach, *balanced* pCASL, uses an identical gradient waveform with a residual moment for both labeling and control experiments. In both methods, RF polarity is alternated in the control sequence and constant in the labeled one[17], as shown in Figure 2.4.

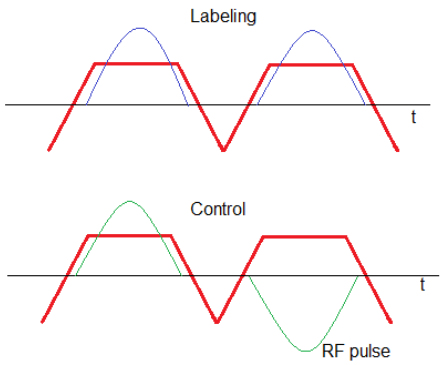

Figure 2.4: A typical balanced pCASL experiment.

The main advantages of these technique are an improvement of the balance labeling efficiency/image SNR, reduced MT effect and power deposition, when comparing with CASL[18].

2.1.4 Velocity Selective Arterial Spin Labeling

Velocity Selective ASL (VS-ASL), contrary to all methods previously depicted, does not invert the inflowing blood at a specific location. Instead, VS-ASL consists on saturating the blood moving at a velocity superior to a specified *cutoff* value, to achieve perfusion contrast. With VS-ASL, it is obtained a smaller and more uniform transit delay for the delivery of blood to the target tissue.

In pathologies in which slow or collateral flow conditions may exist, conventional ASL methods that apply magnetic labels at a specific location may not provide robust measures of CBF, as the transit delay for the delivery of blood to target tissues may far exceed the relaxation time of the labeled blood. Figure 2.5 shows a representation of VS-ASL.

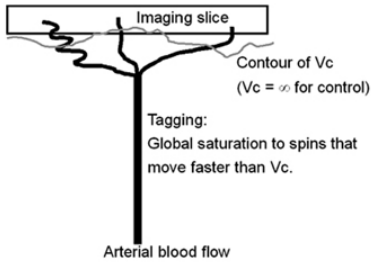

Figure 2.5: A representation of the typical VS-ASL experiment[19].

For the acquisition sequence, it is imposed the condition $V < V_c$, hence the resulting image includes labeled magnetization from spins that have decelerated during TI from above to below V_c, assuming that the velocities in the arterial tree are decreasing[20]. This is an important feature of VS-ASL since it functions as a filter for venous blood. In general, venous blood tends to accelerate, and as a large volume of venous blood is labeled, since it respects $V > V_c$ at the labeling instant, the condition $V < V_c$ will not be respected at the acquisition instant, thus leaving out the contribution of venous blood, that could compromise the validity of this method for obtaining CBF.

In Table 2.1, an overall comparison of all ASL types is presented.

2.2 ASL signal processing methods

As explained in the previous Section, in a typical ASL experiment a series of control and labeled images is acquired. These images are obtained in a alternate sequence, and a perfusion time series can be formed by subtracting labeled and control images[21]. Currently, there are three subtraction methods most commonly used[22]:

- Pair-wise subtraction
- Surround subtraction
- Sinc-interpolated subtraction

Table 2.1: ASL types - advantages and disadvantages.

ASL Type	Advantages	Disadvantages
PASL	High labeling efficiency Lower Specific Absorption Rate (SAR) Improved transit time effects	Lower SNR Increased transit delay
CASL	Higher SNR than PASL Shorter transit delay	Lower labeling efficiency SAR Magnetization Transfer effects Continuous RF transmit hardware required
pCASL	Higher SNR than PASL Higher labeling efficiency than CASL Improved transit time effects	Higher SAR Limited clinical availability
VS-ASL	Ability to measure low CBF	lower SNR

For a better understanding of the different types of subtractions about to be presented, let a set of acquisitions, expressed as an n length vector, be considered as:

$$[C_1, L_1, C_2, L_2, ..., C_{n/2}, L_{n/2}] \tag{2.1}$$

where the control images are identified as C_i and labeled images as L_i, with i varying from 1 to $n/2$. The value of the perfusion, P, can be extracted from this set of images.

2.2.1 Pair-wise subtraction

The Pair-wise subtraction, also known as *Simple Subtraction*, is the simplest method used. In this case, the perfusion is estimated by subtracting to each control image, the labeled image adjacent to it in the acquisition set. By performing this operation, it is expected for the remaining signal to be caused by the arterial labeling[22]. This can be mathematically represented as:

$$[P_1, P_2, ..., P_{n/2}] = [C_1 - L_1, C_2 - L_2, ..., C_{n/2} - L_{n/2}] \tag{2.2}$$

Ideally, the control and labeled images would be acquired at the same instant, but due to practical limitations of the ASL acquisition process, such as necessary transit time of blood from the region of labeling to the acquisition site (representing at least 2s between the acquisition of a labeled image and the next control), it is not feasible. During this period, signal fluctuations can occur, and these may not be attributed to the labeling effect. These signal fluctuations can be caused by random noise or systematic changes in the magnetization of the tissues (the BOLD effect).

2.2.2 Surround subtraction

In order to minimize the contribution from signal unrelated to perfusion, another method of performing the subtraction of control and labeled images was proposed in[23]. In the surround subtraction approach, each control image is subtracted by an average of the previous labeled image and the next labeled image, resulting in a difference signal insensitive to linear trends in the overall signal[23],

$$[P_1, P_2, ..., P_{n/2}] = [C_1 - L_1, C_2 - \frac{L_1 + L_2}{2}, ..., C_{n/2} - \frac{L_{(n/2)-1} + L_{n/2}}{2}] \tag{2.3}$$

High order signal variations, resulting from BOLD contrast will still be present in the difference signal, although with a small contribution.

2.2.3 Sinc-interpolated subtraction

First proposed in[22], the Sinc-interpolated subtraction attempts to remove the signal fluctuation effect caused by the time delay between the control and labeled images. Rather than a new approach, it can be considered as a complement of the Pair-wise subtraction. By doubling the temporal resolution of the labeled images vector through sinc interpolation, it is possible to resample at intermediate points in time, hence estimating the labeled images vector as if they had been acquired at the same time as the control images ($L_{1/2}$, $L_{3/2}$,...). Afterwards, by subtracting control and estimated labeled images, the perfusion vector is obtained.

$$[P_1, P_2, ..., P_{n/2}] = [C_1 - L_{1/2}, C_2 - L_{3/2}, ..., C_{n/2} - L_{n-1/2}] \tag{2.4}$$

The fractional numbers represent the projected time series at a point, one TR earlier in time.

The validity of this processing is based on the assumption that the perfusion signal does not suffer significant alterations in frequencies higher than the Nyquist frequency in the perfusion data. In fact, the lower the TR of data acquisition, the better the adaptability.

In this work, only two of the three signal processing methods will be used to assess and compare the results obtained by the proposed algorithm. These will be (a)*Pair-wise subtraction* and (b)*Surround-subtraction*.

2.3 Alternative Techniques

ASL is not the only technique used to assess information about brain hemodynamics. Many other methods exist, with different characteristics, better suited for a specific type of desired information. An overview of most commonly used techniques is presented in the following section.

Positron Emission Tomography - PET

PET is a non-invasive technique, potentially providing tomographic images of several quantitative parameters describing various aspects of brain hemodynamics - regional CBF (rCBF), regional

CBV (rCBV), cell viability and proliferation or metabolic activity of tissues, among others. The images are obtained by labeling different substances of biological interest with a positron emitting radioisotope (PET radiopharmaceuticals). The most common compounds used for the measure of CBF are $^{15}O_2$, $C^{15}O_2$, $H_2^{15}O_2$, and ^{18}F, and are administrated via intravenous injection or inhalation, depending on the compound used. A schematic of the functioning of a PET exam is displayed in Figure 2.6. PET radiopharmaceuticals are cyclotron products and have a very short

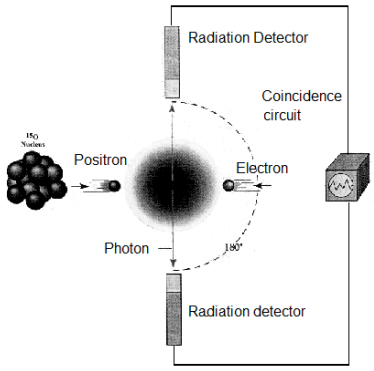

Figure 2.6: A scheme of a PET exam. The system detects pairs of gamma rays emitted indirectly by a positron emitting radioisotope, which is introduced into the body on a biologically active molecule. Three-dimensional images of tracer concentration within the body are then constructed by computer analysis[24].

half-life (^{18}F 1.7 hours; ^{15}O 2 minutes;^{13}N 10 minutes; ^{11}C 20 minutes). Whole body radiation exposure by PET examination is usually 0.5 to 2.0 mSv per scan and the radiation dose may differ among institutions depending on the protocol or quality of the PET camera. Moreover, the duration of the data acquisition depends on the selected method and tracer, though it typically ranges from 5 to 9 minutes for a routine clinical study[25].

Single Photon Emission Computed Tomography - SPECT

SPECT is as nuclear tomographic technique that recurs to the properties of gamma radiation. It is a non-invasive technique that generates 3 dimensional images of the distribution of a specific radiopharmaceutical that can represent regional cerebral hemodynamics.

^{133}Xe is the most antique tracer for measuring the brain hemodynamics, but the gamma rays emitted have low energy, which leads to abundant scatter and, consequently, limited spatial resolution. In order to overcome this problem, other compounds have been used as retention tracer, such as $^{99m}Tc - HMPAO$, $^{99m}Tc - ECD$, and $^{123}I - IMP$. Depending on the tracer used, the effective dosage can vary from 3.53mSv to 12.21mSv.

Using this retention tracers, the goal of the exam is to achieve a total of > 5 million counts, that can take the duration of SPECT scan to go from 10 to 15 minutes.

A representation of the data acquisition in a SPECT exam is shown in Figure 2.7.

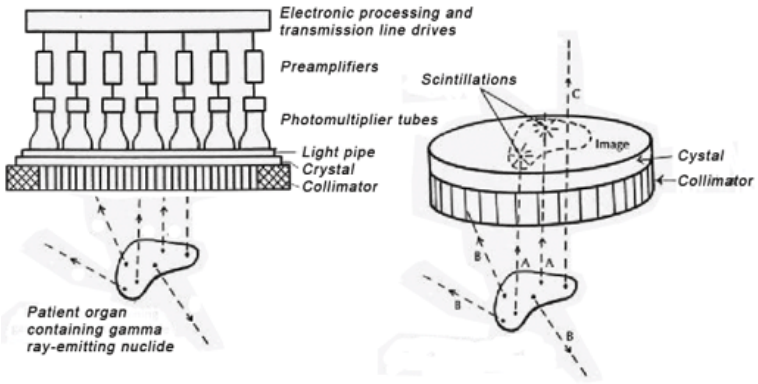

Figure 2.7: A scheme of a SPECT exam. SPECT imaging is performed by using a gamma camera to acquire multiple 2-D images (also called projections), from multiple angles, of the gamma emission of the isotope[24].

Blood-Oxygenation Level Dependent - BOLD

The BOLD-MRI signal arises from the liberation by the oxyhemoglobin (diamagnetic) of its oxygen, originating a deoxyhemoglobin molecule (paramagnetic). This presence of paramagnetic molecules in the blood produces a difference in the magnetic susceptibility between blood vessels and surrounding tissue[26]. When a susceptibility-induced local field differences exist within an imaging voxel, there is distribution of shifts in the water molecules resonance frequencies. This distribution reduces the signal intensity and the voxel darkens in the image. These intensity losses are the source of the BOLD contrast. Since BOLD depends on the state of blood oxygenation, physiological events that change the oxy/deoxyhemoglobin ratio can be detected by the accentuation of BOLD contrast in the imaging, in a non-invasive manner. Figure 2.8 presents a summary of BOLD contrast.

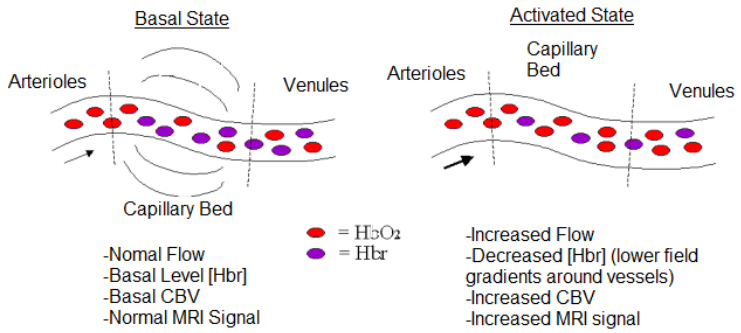

Figure 2.8: The bases of BOLD contrast[27].

In Table 2.2 the main strengths and weaknesses of each method are presented.

Table 2.2: Advantages and disadvantages of the techniques used to measure brain haemodynamics (ASL, PET, SPECT and BOLD)[25].

Method	Advantages	Disadvantages
ASL	Repeatability (lack of ionizing radiation) Non-invasive Flexibility (trade-off between spatial resolution and imaging time)	CBF underestimation (due to delayed arrival of Arterial Blood) Low SNR MRI constraints (contraindications, claustrophobia...)
PET	Accurate quantitative measurements Different ligands allow the study of different factors	Radioactivity Impossible to use in emergency settings Requirement of insite cyclotron for production of CBF tracers High Cost (although high cost-effectiveness)
SPECT	^{99m}Tc generator widely available Can be used at bedside and in emergency setting Low cost	Radioactivity No quantitative measurements Poor spatial resolution
BOLD	Repeatability (lack of ionizing radiation) Non-invasive High SNR	Not a direct measure of CBF MRI constraints (contraindications, claustrophobia...)

Chapter 3

Problem Formulation

This Chapter is dedicated to the mathematical considerations and algorithm implementation. In Section 3.1 the mathematical model used for representing ASL image estimation problem is presented, followed by the the algorithm implementation steps in Section 3.2.

In order to compare the algorithm, the two methods selected in the previous Chapter were also adapted for implementation, as shown in Section 3.3.

3.1 Mathematical model

Let $Y(t)$ be a sequence of L PASL images with $N \times M$ pixels. The observation model which will be considered throughout this work is

$$Y(t) = F + D(t) + v(t)\Delta M + \Gamma(t) \tag{3.1}$$

where $t \in 1, 2, ..., L$ is an image index, $Y(t)$ is the t^{th} noisy image within the sequence, F is a time invariant $N \times M$ image describing the static magnetization of the tissues, $D(t)$ is as slow variant image describing the baseline fluctuations of the signal over time (called *Drift*), and ΔM is the magnetization variation in the tissues caused by the alternate inversion process occurring at each *Inversion Time* (TI). $v(t)$ is a binary signal indicating the labeled periods related to the inversion process, as shown in figure 3.1. The image $\Gamma(t) = \gamma_{ij}(t)$ is assumed to be *Additive White Gaussian Noise* (AWGN)[28, 29], where $\gamma_{ij} \sim \mathcal{N}\left(0, \sigma_y^2\right)$ are stationary independent and identically distributed (iid) random variables with Gaussian distribution.

3.2 Algorithm implementation

In order to simplify the problem formulation and algorithm design it will be considered the following alternative formulation for the observation model described in equation (3.1)

$$\mathbf{Y} = \mathbf{f}\mathbf{u}^T + \mathbf{D} + \mathbf{\Delta}\mathbf{m}\mathbf{v}^T + \mathbf{\Gamma} \tag{3.2}$$

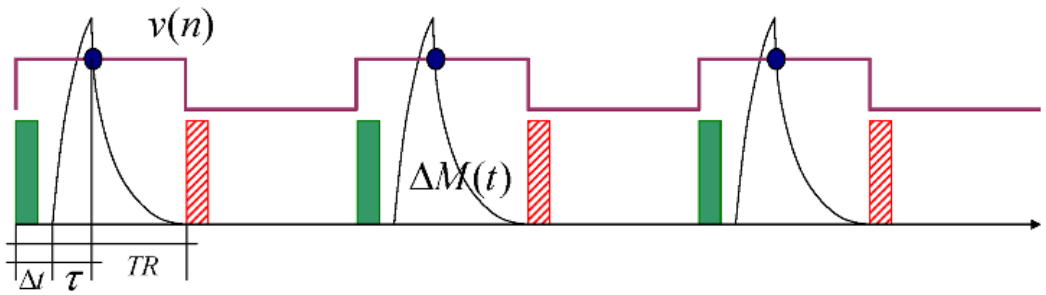

Figure 3.1: Schematics of PASL labeling strategy. The rectangular signal (purple) represents $v(t)$, and its value is equal to one for labeling acquisition and zero for a non-labeling acquisition. Δt is the time delay between the labeling of the arterial blood and reaching the tissues, τ is the instant where the acquisition is made, and TR is the time period before another sequence of labeling or non labeling can occur.

where the t^{th} columns of $\mathbf{Y}, \mathbf{D}$ and $\mathbf{\Gamma}$ are vectorized versions of the corresponding images, arranged by *lexicographic* order of their pixel index[30].

In practice, the images of the sequence, after vectorization, are stacked in $NM \times L$ matrices. The time invariant images F and ΔM, after vectorization, give rise to the $NM \times 1$ column vectors $\mathbf{f}$ and $\Delta\mathbf{m}$, respectively. The L length signal $v(t)$ is represented by the $L \times 1$ column vector $\mathbf{v}$. The vector $\mathbf{u}$ is a constant matrix of ones. The probability of $\mathbf{Y}$ is a multivariate Gaussian distribution with mean $\mu = \mathbf{f}\mathbf{u}^T + \mathbf{D} + \mathbf{\Delta}\mathbf{m}\mathbf{v}^T$ and covariance diagonal matrix, $\sigma_y^2\mathbf{I}$, since the noise is white,

$$p(\mathbf{Y}) \sim \mathcal{N}(\mu, \sigma_y^2\mathbf{I}). \tag{3.3}$$

The *Maximum Likelihood* (ML) estimation of the unknown images, $\theta = \{\mathbf{f}, \mathbf{D}, \mathbf{\Delta}\mathbf{m}\}$, may be formulated as follows:

$$\theta = \arg\min_{\theta} E_y(\mathbf{Y}, \mathbf{v}, \theta) \tag{3.4}$$

where the energy function

$$\begin{aligned} E_y(\mathbf{Y}, \mathbf{v}, \theta) &= -\log p(Y|\theta, \mathbf{v}) \\ &= ||\mathbf{f}\mathbf{u}^T + \mathbf{D} + \mathbf{\Delta}\mathbf{m}\mathbf{v}^T - \mathbf{Y}||^2 + C \end{aligned} \tag{3.5}$$

is called *Data Fidelity Term*.

The optimization task described in equation 3.4 is an *ill-posed* problem[4] and regularization is needed. By using the *maximum a posteriori* (MAP) criterion the regularization is introduced by the prior distribution of the parameters. In this approach, the new energy function to be minimized is $E(\mathbf{Y}, \mathbf{v}, \theta) = -\log p(\mathbf{Y}|\theta, \mathbf{v})p(\theta)$ and the estimation process is formulated as follows,

$$\theta = \arg\min_{\theta} E(\mathbf{Y}, \mathbf{v}, \theta) \tag{3.6}$$

where

$$E(\mathbf{Y}, \mathbf{v}, \theta) = E_y(\mathbf{Y}, \mathbf{v}, \theta) + E_\theta(\theta) \tag{3.7}$$

with $E_\theta(\theta) = -\log p(\theta)$. Since the parameters $\mathbf{f}$, $\mathbf{D}$ and $\mathbf{\Delta m}$ in θ are assumed independent, the prior term can be decomposed,

$$E_\theta(\theta) = E_f(\mathbf{f}) + E_D(\mathbf{D}) + E_{\Delta M}(\mathbf{\Delta m}). \tag{3.8}$$

Here, the parameter images $\mathbf{f}$, $\mathbf{D}$ and $\mathbf{\Delta m}$ in θ are considered *Markov Random Fields*, which means its priors are Gibbs distributions[4],

$$p(\tau) = \frac{1}{Z_\tau} e^{-U(\tau)} \tag{3.9}$$

where $U(\tau)$ is called *Gibbs* energy with $\tau \in \{\mathbf{f}, \mathbf{D}, \mathbf{\Delta m}\}$. The *Gibbs* energy for 2D images is given by

$$U(\tau) = \sum_i \left(\delta_h^2(i) + \delta_v^2(i)\right) \tag{3.10}$$

where i is the index of each pixel of the image and $\delta_h(i)$ and $\delta_v(i)$ are the differences of the i^{th} pixel to its horizontal and vertical neighbors, respectively.

In case of time varying *Drift* imaged, $\mathbf{D}$, a third term is added to account for the temporal dimension

$$U(\mathbf{D}) = \sum_i \left(\delta_h^2(i) + \delta_v^2(i) + \delta_t^2(i)\right) \tag{3.11}$$

By adding the prior term, the estimation is turned into a well-posed problem. In terms of image quality, the prior term will be responsible for the *smoothness* of the solution. Equation (3.5) has a global minimum, called MAP solution, which is often difficult to calculate, as the MAP optimization may not be convex[4].

Making *a priori* assumptions in the medical field may not be the most correct approach, since it may lead to false premises and therefore incorrect diagnosis. However, it is frequent to assume that the medical images are band-limited and slow changing in space, except near organ boundaries, where sudden transitions are expected to happen. This can be seen as a set of springs that pull the solution towards the data and smooths the solution to avoid fast changes.

The minimization of the energy function, depicted in equation (3.5), is illustrated in figure 3.2.

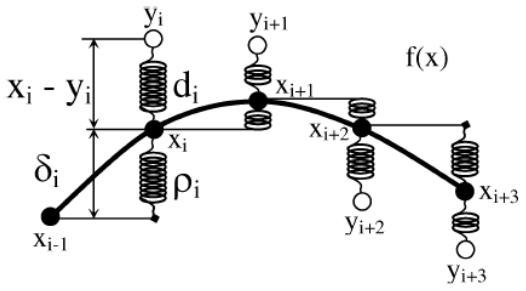

Figure 3.2: Mechanical interpretation of the optimization task. A set of strings "pulls" the solution towards the data[4].

Equation (3.5) can be re-written with all its priors as follows:

$$\begin{aligned} E(\mathbf{Y},\mathbf{f},\mathbf{\Delta m},\mathbf{D}) \quad = & \\ & \tfrac{1}{2\sigma^2} \quad \sum_{i,j=0}^{N-1,M-1} [y(i,j) - f(i,j) - \Delta m(i,j) - d(i,j)] \\ & + \quad \alpha \sum_{i,j=0}^{N-1,M-1} [\varphi_v^2(i,j) + \varphi_h^2(i,j) + \varphi_t^2(i,j,t)] \\ & + \quad \beta \sum_{i,j=0}^{N-1,M-1} [\varrho_v^2(i,j) + \varrho_h^2(i,j)] \\ & + \quad \gamma \sum_{i,j=0}^{N-1,M-1} [\mu_v^2(i,j) + \mu_h^2(i,j)] \end{aligned} \tag{3.12}$$

where $\varphi_v(i,j) = d(i,j) - d(i-1,j)$, $\varrho_v(i,j) = f(i,j) - f(i-1,j)$ and $\mu_v(i,j) = \delta m(i,j) - \delta m(i-1,j)$ are the first-order vertical differences of $\mathbf{D}, \mathbf{f}$ and $\mathbf{\Delta m}$ and $\varphi_h(i,j) = d(i,j) - d(i,j-1)$, $\varrho_v(i,j) = f(i,j) - f(i,j-1)$ and $\mu_v(i,j) = \delta m(i,j) - \delta m(i,j-1)$ as the first-order horizontal differences of the same elements. $\varphi_t^2(i,j,t) = d(i,j,t) - d(i,j,t-1)$ computes the difference among consecutive pixels in the time frame and represents the temporal prior term.

The parameters α, β and γ are the priors hyper-parameters, relative to $\mathbf{d}$, $\mathbf{f}$ and $\mathbf{\Delta m}$, respectively. Although these may be automatically estimated[31], in this work they were calculated on a trial and error basis.

From this point on, a series of matrix calculations will be executed in order to obtain the final formulae that will allow us to calculate the optimal solution. Only the most relevant steps will be presented.

Starting with equation (3.12), which can be seen as:

$$\begin{aligned} E \quad & (\mathbf{Y},\mathbf{\Delta m},\mathbf{f},\mathbf{D}) = \\ \tfrac{1}{2}\,Tr \quad & \left[(\mathbf{Y} - \mathbf{f}\mathbf{u}^\mathbf{T} - \mathbf{\Delta m}\mathbf{v}^\mathbf{T})^T(\mathbf{Y} - \mathbf{f}\mathbf{u}^\mathbf{T} - \mathbf{\Delta m}\mathbf{v}^\mathbf{T})\right] \\ + \quad & \alpha\, Tr\left[(\phi_h\mathbf{D})^\mathbf{T}(\phi_h\mathbf{D}) + (\phi_v\mathbf{D})^\mathbf{T}(\phi_v\mathbf{D}) + (\mathbf{D}\phi_t)^\mathbf{T}(\mathbf{D}\phi_t)\right] \\ + \quad & \beta\, Tr[(\phi_h\mathbf{f})^\mathbf{T}(\phi_h\mathbf{f}) + (\phi_v\mathbf{f})^\mathbf{T}(\phi_v\mathbf{f})] \\ + \quad & \gamma\, Tr[(\phi_h\mathbf{\Delta m})^\mathbf{T}(\phi_h\mathbf{\Delta m}) + (\phi_v\mathbf{\Delta m})^\mathbf{T}(\phi_v\mathbf{\Delta m})] \end{aligned} \tag{3.13}$$

and ϕ_h and ϕ_v are $MN \times MN$ matrices used to compute the horizontal and vertical first order differences. Note that Tr stands for the trace of a matrix. Both matrices, ϕ_h and ϕ_v, have the following structure.

$$\phi = \begin{pmatrix} 1 & 0 & 0 & \dots & \dots & 0 & 0 & -1 \\ -1 & 1 & 0 & \dots & \dots & \dots & 0 & 0 \\ 0 & -1 & 1 & \dots & \dots & \dots & 0 & 0 \\ \dots & \dots & \dots & \dots & \dots & -1 & 1 & 0 \\ 0 & 0 & 0 & \dots & \dots & 0 & -1 & 1 \end{pmatrix} \tag{3.14}$$

From equation (3.13)

$$\begin{aligned} E \quad & (\mathbf{Y}, \mathbf{\Delta m}, \mathbf{f}, \mathbf{D}) = \\ \tfrac{1}{2}Tr \quad & \left[(\mathbf{Y} - \mathbf{fu^T} - \mathbf{\Delta m v^T})^T (\mathbf{Y} - \mathbf{fu^T} - \mathbf{\Delta m v^T})\right] \\ + \quad & \alpha Tr\left[(\mathbf{D^T}(\phi_h^\mathbf{T}\phi_h)\mathbf{D} + \mathbf{D^T}(\phi_v^\mathbf{T}\phi_v)\mathbf{D} + \mathbf{D}(\phi_t^\mathbf{T}\phi_t)\mathbf{D^T}\right] \\ + \quad & \beta Tr[\mathbf{f^T}(\phi_h^\mathbf{T}\phi_h)\mathbf{f} + \mathbf{f^T}(\phi_v^\mathbf{T}\phi_v)\mathbf{f}] \\ + \quad & \gamma Tr[\mathbf{\Delta m^T}(\phi_h^\mathbf{T}\phi_h)\mathbf{\Delta m} + \mathbf{\Delta m^T}(\phi_v^\mathbf{T}\phi_v)\mathbf{\Delta m}] \end{aligned} \tag{3.15}$$

Considering $\Phi_h = \phi_h^T\phi_h$, $\Phi_v = \phi_v^T\phi_v$ and $\Phi_t = \phi_t^T\phi_t$ equation 3.15 can be re-written as:

$$\begin{aligned} E \quad & (\mathbf{Y}, \mathbf{\Delta m}, \mathbf{f}, \mathbf{D}) = \\ \tfrac{1}{2}Tr \quad & \left[(\mathbf{Y} - \mathbf{fu^T} - \mathbf{\Delta m v^T})^T (\mathbf{Y} - \mathbf{fu^T} - \mathbf{\Delta m v^T})\right] \\ + \quad & \alpha Tr\left[(\mathbf{D^T}(\mathbf{\Phi}_h + \mathbf{\Phi}_v)\mathbf{D} + \mathbf{D}(\mathbf{\Phi}_t)\mathbf{D^T}\right] \\ + \quad & \beta Tr[\mathbf{f^T}(\mathbf{\Phi}_h + \mathbf{\Phi}_v)f] \\ + \quad & \gamma Tr[\mathbf{\Delta m^T}(\mathbf{\Phi}_h + \mathbf{\Phi}_v)\mathbf{\Delta m}] \end{aligned} \tag{3.16}$$

Making a final consideration, $\Theta = \Phi_h + \Phi_v$, initial equation (3.12) now stands as

$$\begin{aligned} E \quad & (\mathbf{Y}, \mathbf{\Delta m}, \mathbf{f}, \mathbf{D}) = \\ \tfrac{1}{2}Tr \quad & \left[(\mathbf{Y} - \mathbf{fu^T} - \mathbf{\Delta m v^T})^T (\mathbf{Y} - \mathbf{fu^T} - \mathbf{\Delta m v^T})\right] \\ + \quad & Tr\left[\alpha_1(\mathbf{D^T\Theta D} + \alpha_\mathbf{2}\mathbf{D}(\mathbf{\Phi}_t)\mathbf{D^T}\right] \\ + \quad & Tr[\beta\mathbf{f^T\Theta}f + \gamma\mathbf{\Delta m^T\Theta\Delta m}] \end{aligned} \tag{3.17}$$

Computing the first derivative of E to the first two unknowns of the system

$$\begin{cases} \nabla_\mathbf{f} E &= (\mathbf{D} + \mathbf{fu^T} + \mathbf{\Delta m v^T} - \mathbf{Y})\mathbf{u} + \beta\Theta^T\mathbf{f} \\ \nabla_{\mathbf{\Delta m}} E &= (\mathbf{D} + \mathbf{fu^T} + \mathbf{\Delta m v^T} - \mathbf{Y})\mathbf{v} + \gamma\Theta^T\mathbf{\Delta m} \end{cases} \tag{3.18}$$

As mentioned before, the MAP solution has a global minimum. The minimizers of equation(3.17) can be computed by finding the stationary points of the energy function,

$$\begin{cases} \nabla_\mathbf{f} E &= 0 \\ \nabla_{\mathbf{\Delta m}} E &= 0 \end{cases} \tag{3.19}$$

From equation(3.18) and (3.19), we obtain the equations

$$\begin{cases} \mathbf{fu^T u} + \mathbf{\Delta m v^T u} + \beta\mathbf{\Theta^T f} &= (\mathbf{Y} - \mathbf{D})\mathbf{u} \\ \mathbf{fu^T v} + \mathbf{\Delta m v^T v} + \gamma\mathbf{\Theta^T\Delta m} &= (\mathbf{Y} - \mathbf{D})\mathbf{v} \end{cases} \tag{3.20}$$

Considering the following simplifications

$$\begin{aligned}
\mathbf{A_f} &= (l\mathbf{I} + \beta\mathbf{\Theta}^T) && (3.21)\\
\mathbf{a_f} &= (\mathbf{Y} - \mathbf{D})\mathbf{u} && (3.22)\\
a_m &= \mathbf{v^T u} && (3.23)\\
\mathbf{A_m} &= ((\mathbf{v^T v})\mathbf{I} + \gamma\mathbf{\Theta^T}) && (3.24)\\
\mathbf{a_m} &= (\mathbf{Y} - \mathbf{D})\mathbf{v} && (3.25)\\
a_f &= \mathbf{u^T v} && (3.26)
\end{aligned}$$

and applying them to equation system(3.20)

$$\begin{cases} \mathbf{A_f f} + a_m\mathbf{\Delta m} &= \mathbf{a_f} \\ a_f\mathbf{f} + \mathbf{A_m}\mathbf{\Delta m} &= \mathbf{a_m} \end{cases} \quad (3.27)$$

which is now a simple two equation with two unknowns. The solution to this system is

$$\begin{cases} \hat{\Delta m}(\mathbf{D}) &= (a_f a_m\mathbf{I} - \mathbf{A_f A_m})^{-1}(a_f\mathbf{a_f}(\mathbf{D}) - \mathbf{A_f a_m}(\mathbf{D})) \\ \hat{f}(\mathbf{D}) &= (a_m a_f\mathbf{I} - \mathbf{A_m A_f})^{-1}(a_m\mathbf{a_m}(\mathbf{D}) - \mathbf{A_m a_f}(\mathbf{D})) \end{cases} \quad (3.28)$$

For the estimation of $\mathbf{D}$, the third unknown of 3.17, it is possible to calculate the partial derivative of E to $\mathbf{D}$

$$\nabla_D E = (\mathbf{D} + \mathbf{fu^T} + \mathbf{\Delta m v^T} - \mathbf{Y}) + \alpha_1\mathbf{\Theta^T D} + \alpha_2\mathbf{D\Phi_t} \quad (3.29)$$

In order to find the global minimum of the MAP solution, equation(3.29) can be re-written as

$$\mathbf{ID} + \alpha_1\mathbf{\Theta^T D} + \alpha_2\mathbf{D\Phi_t} = \mathbf{Y} - \mathbf{fu^T} - \mathbf{\Delta m v^T} \quad (3.30)$$

By weight-splitting $\mathbf{D}$ in equation(3.30),

$$(\xi\mathbf{I}_{nm})\mathbf{D} + (1-\xi)\mathbf{DI}_l + \alpha_1\mathbf{\Theta^T D} + \alpha_2\mathbf{D\Phi_t} = \mathbf{Y} - \mathbf{fu^T} - \mathbf{\Delta m v^T} \quad (3.31)$$

where $\mathbf{I}_{nm}$ and $\mathbf{I}_l$ are identity matrices of order nm and l orders, respectively. Factorizing D,

$$(\xi\mathbf{I} + \alpha_1\mathbf{\Theta^T})\mathbf{D} + \mathbf{D}((1-\xi)\mathbf{I} + \alpha_2\mathbf{\Phi_t}) = \mathbf{Y} - \mathbf{fu^T} - \mathbf{\Delta m v^T} \quad (3.32)$$

Through mathematical manipulation, it is possible to consider

$$\begin{aligned}
\mathbf{A} &= \xi\mathbf{I} + \alpha_1\mathbf{\Theta^T} && (3.33)\\
\mathbf{B} &= ((1-\xi)\mathbf{I} + \alpha_2\mathbf{\Phi_t}) && (3.34)\\
\mathbf{C} &= -\mathbf{Y} - \mathbf{fu^T} - \mathbf{\Delta m v^T} && (3.35)
\end{aligned}$$

and equation(3.32) now stands as

$$\mathbf{AD} + \mathbf{DB} + \mathbf{C} = \mathbf{0} \quad (3.36)$$

Equation(3.36) is a particular case of the *Sylvester-Lyapunov* equation, which is a well-known mathematical framework, commonly used in control theory[4, 32, 33].

The formulas that allow the estimation of the matrices was then inserted in a *MATLAB*® program, which iteratively solved the estimation problem. The algorithm was designed so that on the k^{th} iteration, the estimation of $\mathbf{\Delta m}$ and $\mathbf{f}$ can depend on the value of $\mathbf{D}$ on the $(k-1)^{th}$ iteration. Schematically,

$$\begin{aligned}
&\mathbf{D}_0 = \emptyset \\
&While\ k \\
&\quad \mathbf{\Delta m}_k(\mathbf{D}_{k-1}) \\
&\quad \mathbf{f}_k(\mathbf{D}_{k-1}) \\
&\quad \mathbf{D}_k(\mathbf{\Delta m}_k, \mathbf{f}_k) \\
&end
\end{aligned} \tag{3.37}$$

3.3 Pair-wise and surround subtractions implementation

After having implemented the proposed algorithm, the two subtraction methods most commonly used in the literature were also adapted to the considered problem formulation for comparison. Based on (3.1), they were introduced as follows:

Pair-wise subtraction

$$\mathbf{\Delta m} = \frac{\sum_{i=1,2}^{l-1} Y(i) - Y(i+1)}{l/2} \tag{3.38}$$

Surround subtraction

$$\mathbf{\Delta m} = \frac{Y(1) - Y(2) + \sum_{i=3,2}^{l-1} (Y(i) - \frac{Y(i-1)+Y(i+2)}{2})}{l/2} \tag{3.39}$$

Chapter 4

Experimental Results and Discussion

Once the equations necessary for the image estimation were obtained, they were implemented in *Matlab*®. The created algorithm was tested with synthetic data and real data and the results were compared to those obtained using Pair-wise and Surround Subtraction (also implemented in *Matlab*®) as described in Chapter 3. The optimal values for the priors were initially calculated, and selected based on the best results obtained, and are depicted in Section 4.1. Subsequently, Monte Carlo simulations were performed at different noise levels in order to test the performance of the proposed algorithm, relative to the standard subtraction methods.

In the final section of this Chapter, the algorithm was applied to real ASL data.

4.1 Synthetic Data

Synthetic ASL data were generated based on a test object with structure similar to the human brain: one axial slice of a real brain mask, segmented into two main regions, *White Matter*(WM) and *Gray Matter*(GM) was used, as shown in Figure 4.1. The relative perfusion intensity of each region was defined for each experiment as described in the following.

Simulation Parameters

As a first step towards the validation of the proposed algorithm, all the parameters of the bayesian algorithm were set to 0. The value of the noise (σ) was set to 1, which adds AWGN with mean value and standard deviation equal to 1, and the magnetization difference ($\mathbf{\Delta M}$) was set to 1 for the GM and 0.5 for the WM. This represents a noise intensity similar to the intensity of the signal, as expected in the real case (mentioned in Chapter 1). The drift signal ($\mathbf{D}$) is a slow-varying cosine, between -1 and 1, and the background intensity of the image ($\mathbf{F}$) is 10000. These parameters

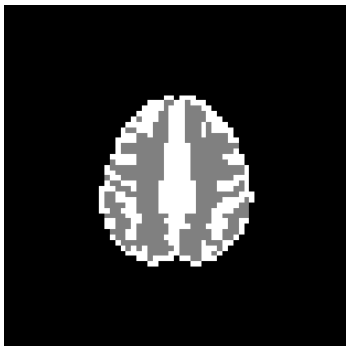

Figure 4.1: Synthetic data test object, derived from a real brain mask (64×64 matrix size). The two different regions, colored in white and gray, represent the white and gray matter of the human brain.

were kept unaltered throughout the tests, with the exception of the noise level. In Figure 4.2, it is presented an image representation of a control acquisition and a labeled acquisition, after the addition of the noise.

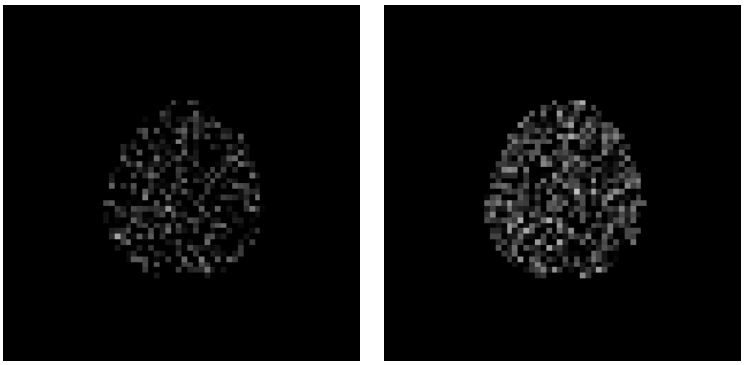

Figure 4.2: A control (left) and a labeling acquisition (right) using synthetic data.

Figure 4.3 presents yet another perspective of the noise corrupting a labeled acquisition, by comparing it with the original labeling in Figure 4.1. In both Figures 4.2 and 4.3, the labeling is

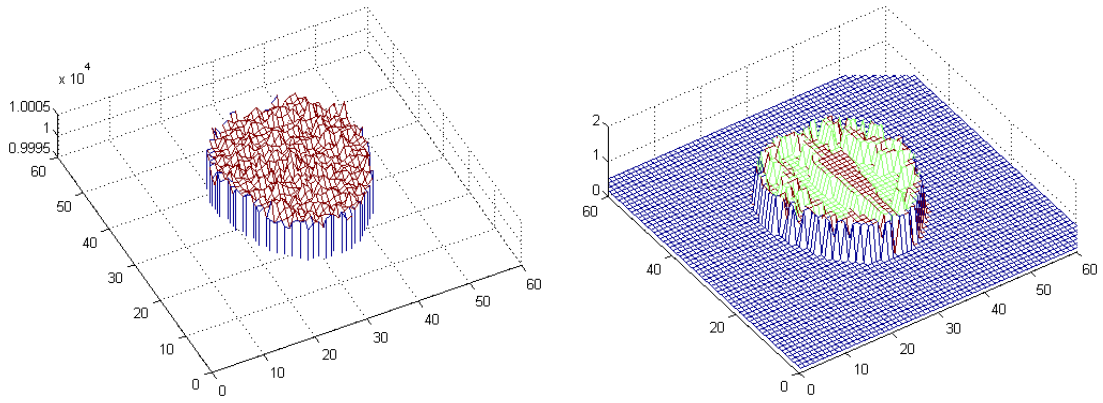

Figure 4.3: A labeled acquisition corrupted with noise (left) and the original labeled regions (right).

not visible in the acquired image, as it tends to disappear in the noise corrupting the image.

Having simulated the acquisition of 50 labeled images and 50 controls, the vector of images was processed with the 3 methods, and the results are shown in Figure 4.4.

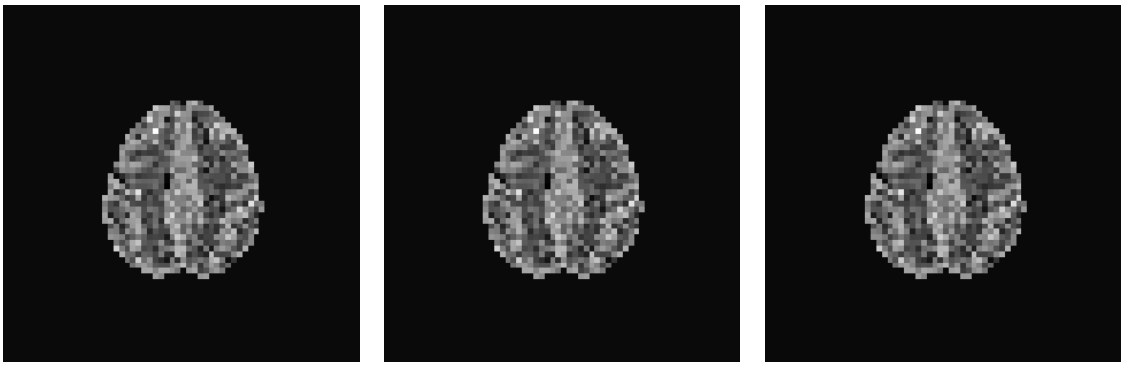

Figure 4.4: Images obtained with the three signal processing methods: proposed algorithm, with priors equal to zero (left), pair-wise subtraction (center) and surround subtraction (right).

The quantitative assessment of the proposed algorithm performance was expressed in terms of *Improved SNR*(dB) (ISNR) and Mean Error(%) (ME). The ISNR is obtained by subtracting the SNR of the image acquired pre-processing (SNR_i) to the value of the SNR obtained post-processing (SNR_f), $ISNR = SNR_f - SNR_i$ (dB). The SNR of the pre and post-processing images is calculated as shown in equation (4.1),

$$SNR = \left(\frac{A_{signal}}{A_{noise}}\right)^2 \tag{4.1}$$

where A_{signal} and A_{noise} are the amplitude of the signal and noise, respectively. On the other hand, the value of the ME of the estimated image is calculated according to equation (4.2)

$$ME(\%) = \frac{100}{N \times M} \sum_{i=1,j=1}^{N,M} \frac{|\hat{x}_{i,j} - x_{i,j}|}{x_{i,j}} \tag{4.2}$$

where N and M are the dimensions of columns and rows of the matrix image, and $\hat{\mathbf{X}}$ and $\mathbf{X}$ the estimation and the original labeling images, accordingly.

The results obtained in this first experiment are given in Table 4.1 and in Figure 4.5. These are the mean values of the results obtained for ISNR and ME in 200 simulations, performed under the same conditions.

Table 4.1: Mean values of ISNR and ME for the test realized with all priors equal to zero.

Method	ISNR (dB)	Mean error (%)
Proposed algorithm	13.906	24.658
Pair-wise subtraction	13.906	24.658
Surround subtraction	13.999	24.393

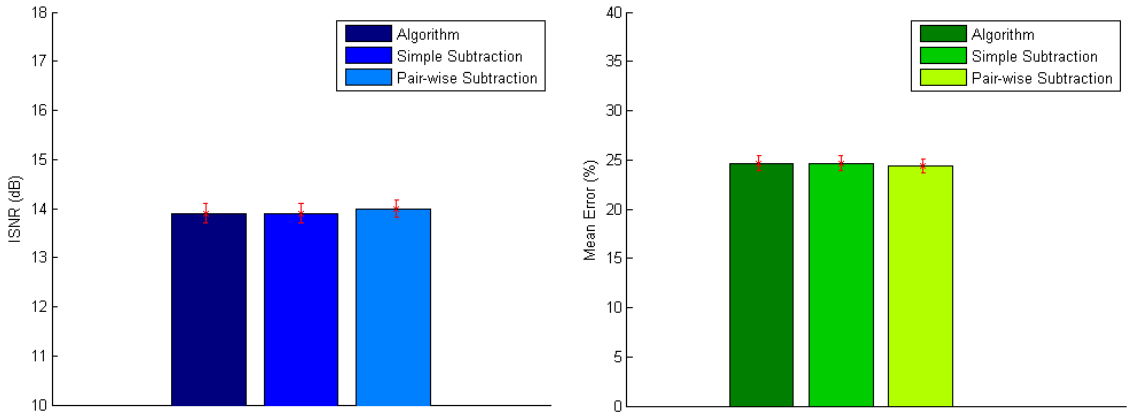

Figure 4.5: Graphical comparison of the values of *ISNR* and *ME* obtained using each of the 3 methods: bars represent the mean and error bars represent the standard deviation.

By comparing the values of Table 4.1, it is clear that in the absence of prior, the proposed algorithm performs exactly like the pair-wise subtraction.

Moreover, surround subtraction performs slightly better, presenting higher ISNR and lower ME. This result was expected, considering that this approach copes best with slow varying drift, as explained in Chapter 2.

Prior optimization

The search for the optimal priors to be used in the upcoming tests was performed on a trial-error basis. Considering equation (3.13), the only priors that are directly related to the image estimation are β and γ (α is related to the drift signal), therefore only these two were optimized.

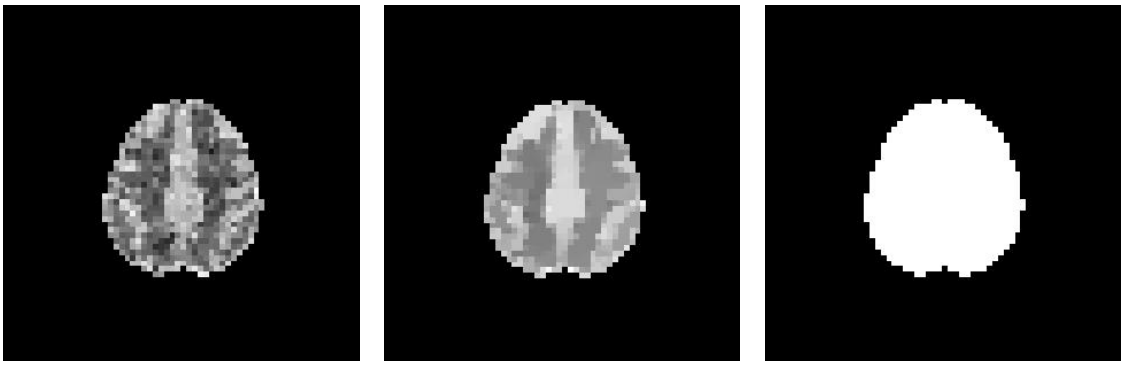

Figure 4.6: Images obtained with different sets of priors. From left to right, less to more rigid imposition.

The selection of the value for the prior is a very delicate process. By choosing a small value, the algorithm might not have sufficient "strength" to pull the solution towards an optimal value and considering an excessively large value, the force pulling towards the solution can cause over-smoothing, as shown in Figure 4.6.

The choice of the optimal value was performed with a dual criteria, which consisted in the selection of the set of parameters that provided higher ISNR, associated with lower ME.

A series of 200 simulations were performed for every set of different values of the priors varying from 0 to 10. For values greater than 10, the prior over-smoothed the resulting image, hence these were not considered. The mean results are presented in Figure 4.7.

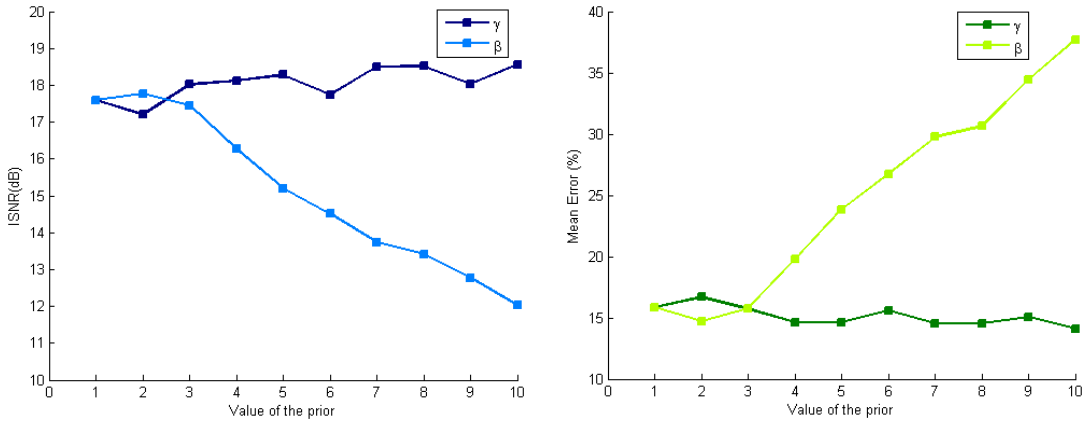

Figure 4.7: In the first graphic, the value of ISNR with ascending values of β and γ. In the second graphic, the corresponding ME.

Evaluating the graphics, it is clear that higher SNR values come from manipulating the value of γ, the prior for ΔM. Among the options, it was selected the value that presented the higher ISNR but at the same time did not compromise the ME of the image. The value of $\gamma = 5$ was selected from the results depicted in Figure 4.8, which shows the evaluation of both parameters of interest, with respect to increasing prior value.

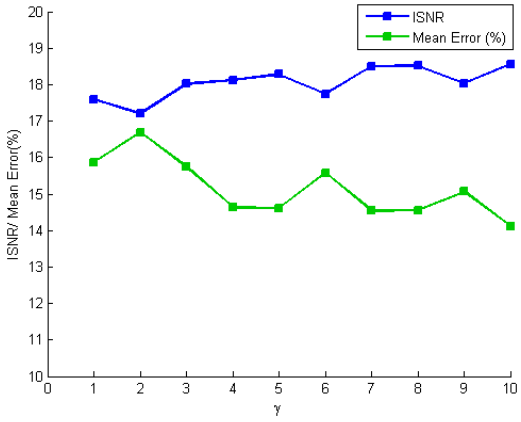

Figure 4.8: Evolution of the values of ISNR and ME of the estimated image with increasing value of γ.

All the remaining priors values were set to 1.

With the chosen values, the proposed algorithm was then tested (200 simulations) against the two subtraction methods and the results are displayed in Figure 4.9

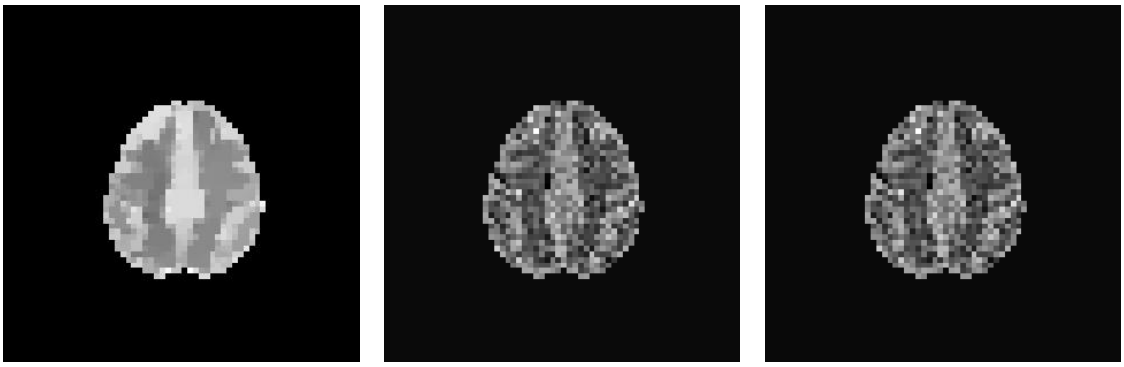

Figure 4.9: Images obtained with the proposed algorithm using the optimized prior (left), pair-wise subtraction (middle) and surround subtraction (right).

In this Figure, it is evident the reduction of the noise corrupting the image. Image areas with the same intensity are more homogeneous in the image obtained with the algorithm than those produced by the common subtraction methods. The edges remain visible and easier to identify. Figures 4.10 and 4.11 represent a spatial perspective of the results and a linear cut through the diagonal of the image, respectively.

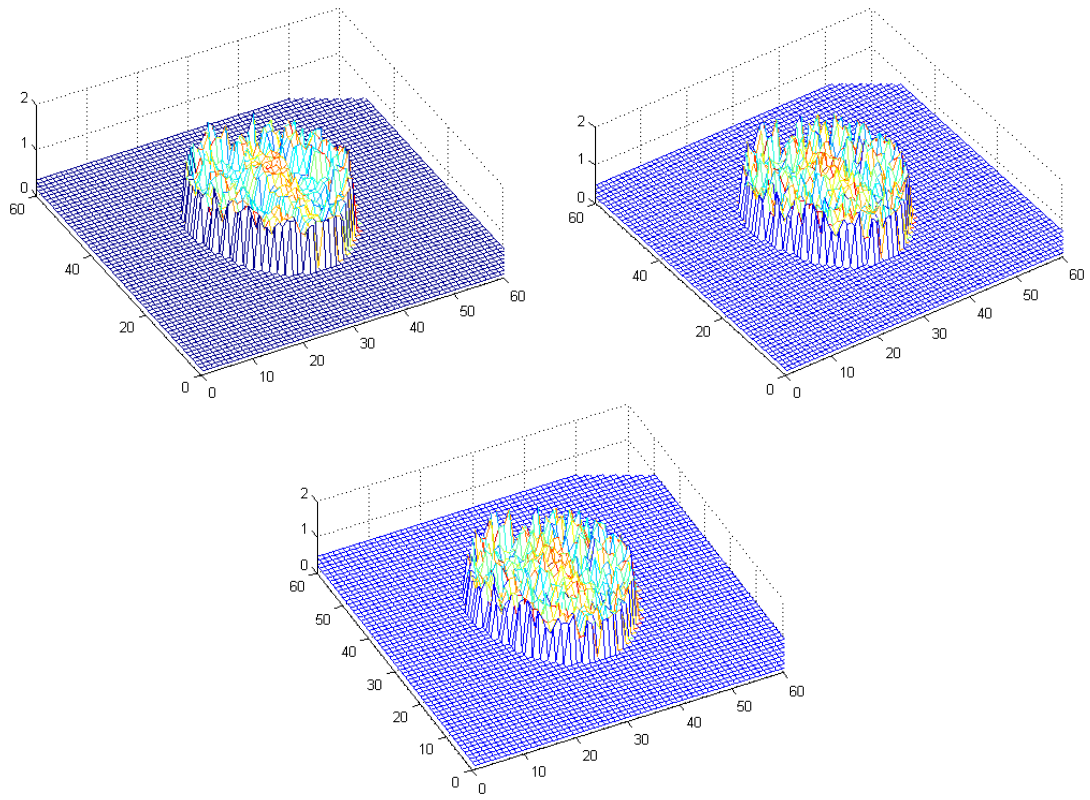

Figure 4.10: Spatial visualization of the images obtained with the proposed algorithm (top left), pair-wise subtraction (top right) and surround subtraction (bottom).

The spikes from the image obtained with the algorithm were reduced as a result of the prior

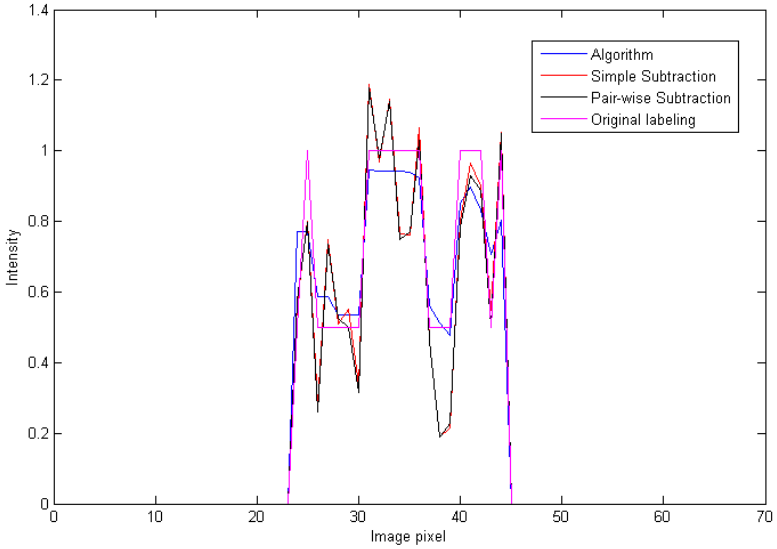

Figure 4.11: Image profile through the diagonal of the estimated image.

pulling towards an optimal solution.

The mean values of ISNR and ME for this test are given in Table 4.2.

Table 4.2: Mean values of ISNR and ME for the test realized with the optimized prior.

Method	ISNR (dB)	Mean error (%)
Proposed algorithm	16.990	17.807
Pair-wise subtraction	14.026	24.492
Surround subtraction	14.103	24.269

In this case, the proposed algorithm obtained an higher value of SNR, approximately $3dB$, and reduced the overall ME by 7%. These values represent an improvement of 23% on SNR and a reduction of ME in aproximately 30%, which expresses an increase of almost one quarter of the total value for the SNR and over a quarter for the redution of ME. The results of Table 4.2 were introduced into a bar graphic, Figure 4.12, for better analysis.

The previous test was the closest approximation to the real case, in which all the parameters replicate the values of the physiological parameters. To study the performance in different noise levels, a series of Monte Carlo simulations (500 for each noise level) were performed. The mean results are shown in Figure 4.13.

For noise levels of 10% of the signal intensity, the traditional subtraction methods performed slightly better than the bayesian algorithm. However, as the noise sistematically increases, the proposed algorithm fastly outperformed the traditional approaches, and at levels of 25%, already the bayesian approach becomes a major advantage. With increasing values of noise, the value of

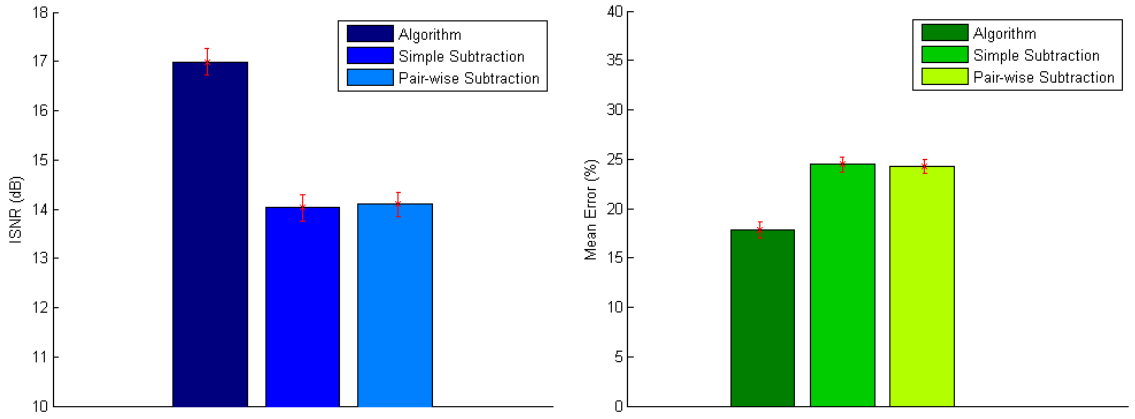

Figure 4.12: Graphical comparison for the values of *ISNR* and *ME* obtained for the 3 methods - prior established situation.

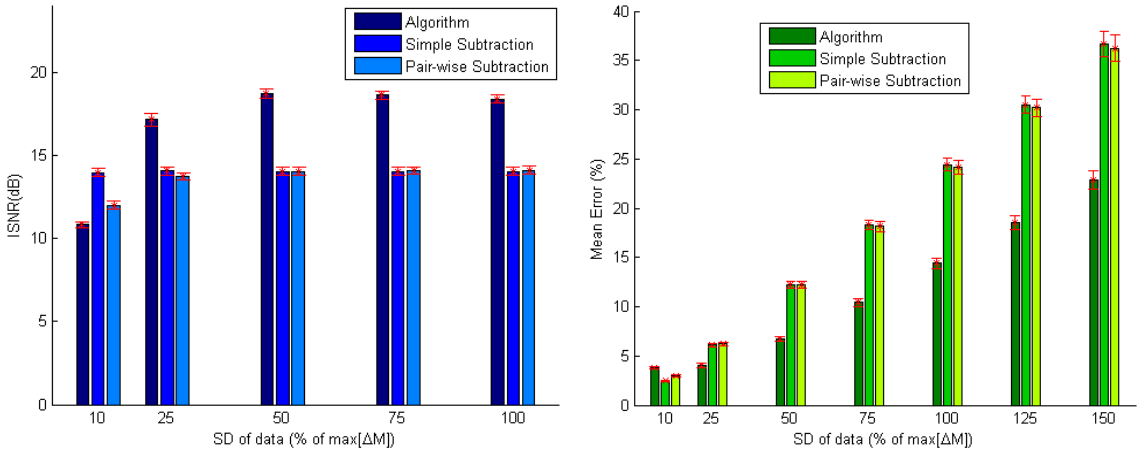

Figure 4.13: Value of ISNR and ME for the three methods, as function of % of noise.

the SNR tends to stabilize, in opposition to the overal ME, which grows systematically, although at a lower rate than for the data driven models.

4.2 Real Data

After testing the proposed algorithm in a set of synthetic data, a set of real acquired images was considered. The real data were acquired from on healthy subject, on a 3T Siemens MRI system (Hospital da Luz, Lisboa) using a PICORE-Q2TIPS PASL sequence[34], with the following parameters: TI1/TI1s/TI2 = 750ms/900ms/1700ms; GE-EPI readout with TR/TE = 2500ms/19ms; 201 repetitions; 9 contiguous axial slices positioned parallel to the AC-PC line, with spatial resolution of $3.5 \times 3.5 \times 7.0$ mm^3 and matrix size $64 \times 64 \times 9$.

Some modifications had to be performed to the proposed algorithm in order to enable the manipulation of these real data, namely the customization of horizontal and vertical difference matrices from equation (3.14) for each slice of the data (the algorithm is only applied to pixels

containing relevant data information, thus excluding all the pixels outside the brain region). Due to the fact that the stopping criteria is no longer available for real data, since one cannot calculate the ME of the estimation with respect to the real value of every pixel in the real data case, the algorithm underwent another transformation, as the stopping criteria became the number of cycle iterations, manually imposed.

Having successfully implemented these alterations, the algorithm was then tested, with the same prior values obtained from the results of synthetic data. Since with the real data set not all the necessary information for the use of the equations (4.1) and (4.2) is available, the results are discussed in a qualitative manner.

Unprocessed control and labeled images are depicted in Figure 4.14.

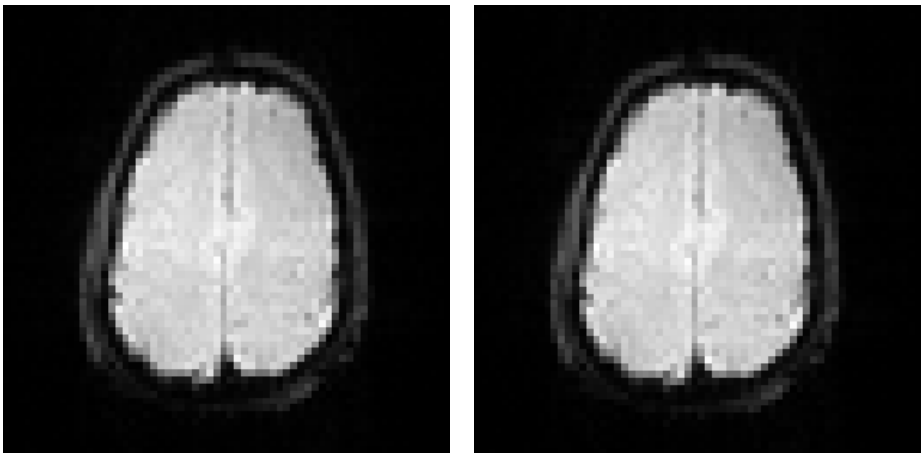

Figure 4.14: Images of a control (left) and labeled (right) acquisitions of one brain slice, acquired from a healthy subject using a PASL sequence on a 3T MRI system.

The first results obtained are depicted in Figure 4.15 and were obtained with 200 iterations of the proposed algorithm. They are compared with the images obtained by pair-wise subtraction and surround subtraction.

Figure 4.15: Images obtained with the proposed algorithm (optimized prior, 200 iterations) (left), pair-wise subtraction (center) and surround subtraction (right).

Analyzing Figure 4.15, the image obtained with the proposed algorithm presents less noise corruption and better distinction of different brain details. Nevertheless, seeking further image improvement, a sequence of tests with different iteration values was then performed. The results obtained are shown in Figure 4.16.

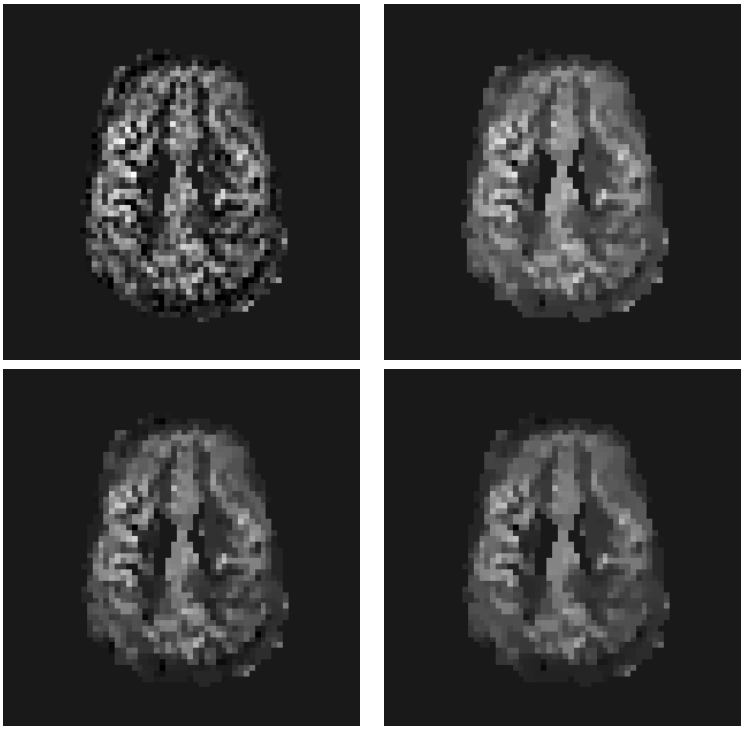

Figure 4.16: Processed images obtained with increasing number of iterations (50, 100, 200 and 400 iterations), from left to right and top to bottom.

The noise removal and image smoothing is observable in Figure 4.16 with increasing iteration number used in the proposed algorithm, and with no compromise of the image edges and transitions.

In Figures 4.17 and 4.18 a comparison of the images resulting from the proposed algorithm, using the optimized prior and number of iterations, and the previously mentioned signal processing methods is shown.

Figure 4.17 displays the resulting improved image quality obtained with the algorithm. The enhancement was obtained at some computational expense, since a larger number of iterations results in a longer processing time. Nevertheless, the purpose of medical imaging is to provide accurate anatomical or functional images and this computational cost is a small disadvantage when compared to the possible advantages that emerge from this new approach.

Figure 4.17: Images obtained with the proposed algorithm (optimized prior, 400 iterations) (left), pair-wise subtraction (center) and surround subtraction (right).

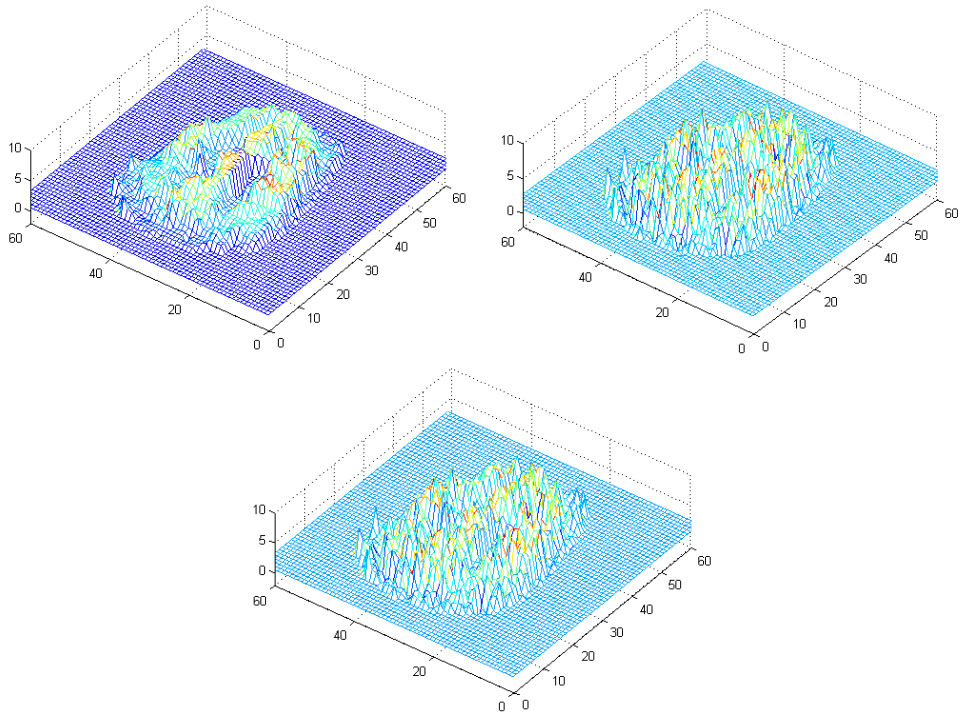

Figure 4.18: A spatial view of images obtained with the proposed algorithm(400 iterations), pair-wise and surround subtraction, respectively.

Chapter 5

Conclusion

Arterial Spin Labeling imaging is a technique to which is recognized great potential, since it can provide useful information about an important physiological parameter, *perfusion*. When comparing ASL to the other perfusion measuring techniques, its main advantages are the non-invasiveness and repeatability, while its main disadvantage is the low intrinsic SNR. In the medical field, as in many others, it is of high interest to obtain the best images possible, and this is the foundation of this thesis. The main objective was to implement a signal processing model to cope with the low SNR of the images produced, as well as improving the overall mean error of the estimation. Currently, ASL images are obtained by subtracting the control and the labeled images, with no further considerations, therefore, considered a data driven approach. The processing method proposed in this thesis incorporates *a priori* knowledge onto the estimation equation, hence improving the quality of the image reconstruction. This *a priori* knowledge is the assumption that no drastic variations of signal along the same tissue are expected, except at the organs boundaries, where signal variations are likely to be intense.

The image estimation problem was formulated in a *bayesian* framework, and after some careful mathematical considerations, the proposed algorithm was implemented and tested on synthetic data. The results obtained, as described in Section 4.1 of Chapter 4, show great improvement in image SNR, approximately 23% increase compared to pair-wise subtraction, as well as a decrease of around 30% in the overall mean error of the estimation, hence fulfilling the objectives initially proposed.

Having determined empirically the optimal prior values with synthetic data, and encouraged by the results obtained, the algorithm was further tested with a set of real data. These images are depicted in Chapter 4, section 4.2, and present less noise corruption, as the smoother shape and sharp frontiers suggest.

Although good results were achieved, the current work opens many possibilities for future work, and some are suggested in the following section.

Future Work

To improve even further image processing or explore the possibilities, some points of particular interest may be approach in future research:

- Automatic prior calculation

  Instead of empirically choosing the numerical value to assign to the priors, on a trial and error basis, the algorithm could be reformulated in order to calculate, on each iteration, the optimal value of the prior.

- Reducing the number of control acquisitions

  One of the major set-backs of ASL is the long duration of the acquisition. For every labeling, a control image is also acquired, in order to minimize the influences of signal fluctuations. However, by decreasing the number of control acquisitions, without compromising image quality, the acquisition time could be reduced. One of the properties of the algorithm proposed is that it also accounts for the presence of temporal drift, hence reducing the need of the label-control sequence for attenuation of this effect.

  For this purpose, testing with sequences other than the strict alternate labeling-control approach could be a mean for reducing acquisition times.

- Validation tests on empirical data

  Further performance analysis on real data sets is necessary in order to achieve the algorithm validation. In particular, it would be of interest to test the performance of the proposed algorithm in terms of the intra- and inter-subject reproducibility of the perfusion estimates, compared to the most common subtraction methodologies.

Bibliography

[1] T.T. Liu and G.G. Brown. Measurement of cerebral perfusion with arterial spin labeling: Part 1. Methods. *Journal of the International Neuropsychological Society*, 13(03):517–525, 2007.

[2] Functional MRI Laboratory University of Michigan. Available from: , $http://fmri.research.umich.edu/research/main\_topics/asl.php$.

[3] I.N. Bankman. *Handbook of medical imaging: processing and analysis*. Academic Pr, 2000.

[4] J.M. Sanches, J.C. Nascimento, and J.S. Marques. Medical image noise reduction using the Sylvester–Lyapunov equation. *IEEE transactions on image processing*, 17(9), 2008.

[5] P. Jezzard, P.M. Matthews, S.M. Smith, et al. *Functional MRI: an introduction to methods*, volume 390. Oxford University Press Oxford, 2001.

[6] F. Bloch. Nuclear induction. *Phys. Rev.*, 70:460–474, Oct 1946.

[7] E. M. Purcell, H. C. Torrey, and R. V. Pound. Resonance absorption by nuclear magnetic moments in a solid. *Phys. Rev.*, 69:37–38, Jan 1946.

[8] F. Calamante, D.L. Thomas, G.S. Pell, J. Wiersma, and R. Turner. Measuring cerebral blood flow using magnetic resonance imaging techniques. *Journal of cerebral blood flow & metabolism*, 19(7):701–735, 1999.

[9] J.A. Detre. Arterial spin labeled perfusion mri. *Clinical Neurology*, 2008.

[10] J.A. Detre and D.C. Alsop. Perfusion magnetic resonance imaging with continuous arterial spin labeling: methods and clinical applications in the central nervous system. *European journal of radiology*, 30(2):115–124, 1999.

[11] A.C. Guyton and J.E. Hall. *Textbook of medical physiology*. WB Saunders (Philadelphia), 1995.

[12] J.M. Pollock, H. Tan, R.A. Kraft, C.T. Whitlow, J.H. Burdette, and J.A. Maldjian. Arterial Spin Labeled MRI Perfusion Imaging: Clinical Applications. *Magnetic resonance imaging clinics of North America*, 17(2):315, 2009.

[13] R.B. Buxton, L.R. Frank, E.C. Wong, B. Siewert, S. Warach, and R.R. Edelman. A general kinetic model for quantitative perfusion imaging with arterial spin labeling. *Magnetic resonance in medicine*, 40(3):383–396, 1998.

[14] D.S. Williams, J.A. Detre, J.S. Leigh, and A.P. Koretsky. Magnetic resonance imaging of perfusion using spin inversion of arterial water. *Proceedings of the National Academy of Sciences*, 89(1):212, 1992.

[15] ET Petersen, I. Zimine, Y.C.L. Ho, and X. Golay. Non-invasive measurement of perfusion: a critical review of arterial spin labelling techniques. *British journal of radiology*, 79(944):688, 2006.

[16] R.R. Edelman, D.G. Darby, and S. Warach. Qualitative mapping of cerebral blood flow and functional localization with echo-planar mr imaging and signal targeting with alternating radio frequency. *Radiology*, 192:513–520, 1994.

[17] DM Garcia, C. De Bazelaire, and D. Alsop. Pseudo-continuous flow driven adiabatic inversion for arterial spin labeling. In *Proc Int Soc Magn Reson Med*, volume 13, page 37, 2005.

[18] W.C. Wu, M. Fernández-Seara, J.A. Detre, F.W. Wehrli, and J. Wang. A theoretical and experimental investigation of the tagging efficiency of pseudocontinuous arterial spin labeling. *Magnetic Resonance in Medicine*, 58(5):1020–1027, 2007.

[19] W.C. Wu and E.C. Wong. Feasibility of velocity selective arterial spin labeling in functional mri. *Journal of Cerebral Blood Flow & Metabolism*, 27(4):831–838, 2006.

[20] E.C. Wong, M. Cronin, W.C. Wu, B. Inglis, L.R. Frank, and T.T. Liu. Velocity-selective arterial spin labeling. *Magnetic Resonance in Medicine*, 55:1334–1341, 2006.

[21] T.T. Liu and E.C. Wonga. A signal processing model for arterial spin labeling functional MRI. *NeuroImage*, 24:207–215, 2005.

[22] GK Aguirre, JA Detre, E. Zarahn, and DC Alsop. Experimental Design and the Relative Sensitivity of BOLD and Perfusion fMRI. *NeuroImage*, 15:488–500, 2002.

[23] E.C. Wong, R.B. Buxton, and L.R. Frank. Implementation of Quantitative Perfusion Imaging Techniques for Functional Brain Mapping using Pulsed Arterial Spin Labeling. *NMR in Biomedicine*, 10:237–249, 1997.

[24] A. Webb and G.C. Kagadis. *Introduction to biomedical imaging*, volume 30. 2003.

[25] M. Wintermark, M. Sesay, E. Barbier, K. Borbely, W.P. Dillon, J.D. Eastwood, T.C. Glenn, C.B. Grandin, S. Pedraza, J.F. Soustiel, et al. Comparative overview of brain perfusion imaging techniques. *Stroke*, 36(9):e83, 2005.

[26] S. Ogawa, TM Lee, AR Kay, and DW Tank. Brain magnetic resonance imaging with contrast dependent on blood oxygenation. *Proceedings of the National Academy of Sciences*, 87(24):9868, 1990.

[27] Nuffield Department of Clinical Neurosciences FMRIB Centre. Available from:, http://www.fmrib.ox.ac.uk/education/fmri/brief-introduction-to-fmri-physiology.

[28] P. Bao and L. Zhang. Noise reduction for magnetic resonance images via adaptive multiscale products thresholding. *Medical Imaging, IEEE Transactions on*, 22(9):1089–1099, 2003.

[29] ME Alexander, R. Baumgartner, AR Summers, C. Windischberger, M. Klarhoefer, E. Moser, and RL Somorjai. A wavelet-based method for improving signal-to-noise ratio and contrast in MR images. *Magnetic Resonance Imaging*, 18(2):169–180, 2000.

[30] T.K. Moon and W.C. Stirling. *Mathematical methods and algorithms for signal processing*, volume 13. Prentice hall New York, 2000.

[31] S.Z. Li. Close-form solution and parameter selection for convex minimization-based edge-preserving smoothing. *IEEE Transactions on Pattern Analysis and Machine Intelligence*, pages 916–932, 1998.

[32] V. Balakrishnan and E. Feron. Linear matrix inequalities in control theory and applications. *International Journal of Robust and Nonlinear Control*, 6(9/10):896–1099, 1996.

[33] E.T. Petersen, T. Lim, and X. Golay. Model-free arterial spin labeling quantification approach for perfusion MRI. *Magnetic Resonance in Medicine*, 55(2):219–232, 2006.

[34] W.M. Luh, E.C. Wong, P.A. Bandettini, J.S. Hyde, et al. Quipss ii with thin-slice ti 1 periodic saturation: a method for improving accuracy of quantitative perfusion imaging using pulsed arterial spin labeling. *Magnetic resonance in medicine*, 41(6):1246–1254, 1999.